







Open Archive Toulouse Archive Ouverte (OATAO)

OATAO is an open access repository that collects the work of Toulouse researchers and makes it freely available over the web where possible

This is an author's version published in: <http://oatao.univ-toulouse.fr/27955>

Official URL: <https://doi.org/10.1016/j.enconman.2021.114304>

To cite this version:

Ihou Mouko, Hilaire and Romanjek, Krunoslav and Mejri, Mahdi  and Oulfarsi, Mostafa and El Oualid, Soufiane and Malinconi, Pauline and Thimont, Yohann  and Malard, Benoît  and Estournès, Claude  and David, Nicolas and Dauscher, Anne *Manufacturing and performances of silicide-based thermoelectric modules*. (2021) *Energy Conversion and Management*, 242. 114304. ISSN 0196-8904

Any correspondence concerning this service should be sent to the repository administrator: tech-oatao@listes-diff.inp-toulouse.fr

Manufacturing and performances of silicide-based thermoelectric modules

H. Ihou Mouko^{a,*}, K. Romanjek^b, M. Mejri^c, M. Oulfarsi^d, S. El Oualid^d, P. Malinconi^a,
Y. Thimont^c, B. Malard^e, C. Estournès^c, N. David^d, A. Dauscher^d

^a HotBlock OnBoard (HBOB), 43 Chemin du Vieux Chêne, 38240 Meylan, France

^b Université Grenoble Alpes, CEA-LITEN, 17 rue des Martyrs, Grenoble Cedex 38054, France

^c CIRJMAT, Université de Toulouse, CNRS, Université Toulouse 3 – Paul Sabatier, 118 Route de Narbonne, 31062 Toulouse Cedex 9, France

^d Université de Lorraine, CNRS, Institut Jean Lamour, F-54000 Nancy, France

^e CIRJMAT, Université de Toulouse, CNRS, INP-ENSIACET – 4 allée Emile Monso, 31030 Toulouse Cedex 4, France

ARTICLE INFO

Keywords:

Silicide-based thermoelectric materials
Spark plasma sintering
Thermoelectric modules processing
Modules performance and reproducibility
Waste heat recovery
Finite element modelling

ABSTRACT

Silicide-based materials are among the most promising candidates for a mass manufacturing of thermoelectric devices allowing converting waste heat into electricity in the medium temperature range (250–500 °C), as they are formed from abundant, low cost and non-toxic elements while exhibiting good thermoelectric properties. In order to manage the detrimental mismatch of thermal expansion coefficients between the *n* and *p*-type materials constituting the thermoelectric legs, inducing thus thermomechanical stresses, we propose in this paper a new design of modules having a 'half-skeleton' structure. Twenty-two modules consisting of two couples of thermoelectric legs combining *n*-type magnesium silicide Mg₂(Si, Sn) and *p*-type higher manganese silicide have been fabricated according to this design, the thermoelectric materials being manufactured by kilograms. It is clearly shown that all the interfaces present in the modules are free from cracks, oxygen, and diffusion. The remarkable repeatability of the measured thermoelectric performance attests the robustness of our manufacturing process. An average power output of 0.37 W has been achieved, i.e. a power density of 0.95 W/cm², for a temperature difference of 400 °C (hot side temperature of 450 °C), placing our modules at the state of the art level while using simple production tools and materials mass production. Comparing this performance to finite elements modelling, the performance could be even enhanced. Long term stability tests at a given temperature and under cycling conditions in different working atmospheres are underway.

1. Introduction

The search for new non-polluting energy sources, substitutes of primary fossil energies, has become a major challenge for our modern world, especially after the signing of the Kyoto Protocol in 1995 (COP 1). Knowing that a large part of the fossil energies used is even lost, generally as waste heat, for instance internal combustion engines of cars only convert about 30% of the primary energy while the other part is lost as heat in both the exhaust gases or the coolant [1], it becomes interesting to think on how it could be recycled. The use of thermoelectric (TE) devices appears as an elegant way to convert directly this waste heat into useful electricity using the Seebeck effect, with the advantage of having no moving parts insuring silence, scalability, and robustness for a long-term use. They have been used for years for space applications to power spatial probes for a mission far from the Sun [2], and more recently the Curiosity and Perseverance rovers launched on Mars [3].

Terrestrial applications concern the heat recovery for instance in the automotive [4] or aircraft sectors [5], the cement industries [6], and quite recently the sector of micro-generation for powering wireless sensors networks [7] and Internet of Things [8].

Conventional π -shaped TE devices are constituted of a plurality of TE couples (or legs) made of *n*- and *p*-type semiconducting materials connected electrically in series and thermally in parallel. The TE legs are usually sandwiched between two metalized ceramic plates and brazed or soldered on the electrical tracks in order to provide a good electrical and thermal transfer and to insure a high mechanical cohesion of the whole set. The manufacturing and development of efficient and long-term stable TE modules is however a great challenge, especially for middle or high operating temperatures, due both to the TE materials themselves (chemical and mechanical stability problems) and to the presence of numerous interfaces (diffusion, electrical and thermal contact resistances, expansion coefficient compatibilities, problems). Various

* Corresponding author.

E-mail address: hilaire.ihou-mouko@hotblock.fr (H. Ihou Mouko).

TE modules architectures and designs, as well as manufacturing methods have been proposed owing to the improvement in their mechanical robustness, chemical stability and electrical performance [see the recent reviews 9–11, and the references therein].

Industrial terrestrial needs are mainly limited to near room (0–200 °C) and middle (200–500 °C) temperature ranges [12]. For near room temperatures applications, the well-established TE modules are based on bismuth and antimony telluride alloys [13]. However, for medium temperature range applications, very few TE modules are available on the market today, while the need is real and the progress on the materials performance (expressed as the dimensionless TE figure of merit $ZT = S^2T/\rho\kappa$, where T is the absolute temperature, S the Seebeck coefficient, ρ the electrical resistivity, and κ the thermal conductivity) is effective. Indeed, several new promising families of TE materials have been identified during these last two–three decades in this temperature range such as for instance skutterudites [14], Half-Heuslers [15], SnX ($X = \text{Te, Se}$) [16,17] or silicide-based materials [18,19]. More details on the performances of all these materials, as well as others, can be found in recent general reviews [20,21]. Among the silicides family, p -type Higher Manganese Silicide (HMS) and n -type $\text{Mg}_2(\text{Si,Sn})$ solid solutions are particularly promising candidates as they are constituted of non-toxic, Earth-abundant, light, and low cost elements [22,23], while they exhibit high TE performance [18,19]. The objective of much of the recent investigations has clearly been to improve the figure of merit ZT by simultaneously decreasing the electrical resistivity and the thermal conductivity, which is a difficult task, by appropriate doping, band structure and/or microstructure engineering [24,25 and the references inside]. For n -type $\text{Mg}_2(\text{Si,Sn})$ solid solutions, the maximum published ZT values are up to 1.5 around 500 °C, when the materials are doped with Sb [26–28]. The p -type $\text{Mg}_2(\text{Si,Sn})$ materials unfortunately possess lower TE performance, a maximum of 0.6 having been nevertheless recently achieved at 380 °C with the Li element [29]. It is why the n -type $\text{Mg}_2(\text{Si,Sn})$ materials are often combined with p -type HMS (MnSi_{1+x}) materials for the fabrication of TE modules, even if the performance of the HMS is less as they exhibit only ZT values ranging between 0.6 and 0.8 at around 530 °C [18,30–32]. However, problems of thermomechanical stability may arise from the mismatch between the coefficient of thermal expansion of both materials ($12 \cdot 10^{-6} \text{ K}^{-1}$ and $17 \cdot 10^{-6} \text{ K}^{-1}$ for the n and p -type materials, respectively [33]), as it has already been shown for such modules [34]. To try to solve this problem, Skomedal et al. [34] have manufactured TE modules using electrical contacts with springs. The springs provide pressure on the TE legs to maintain thermal and electrical contact and ensure flexibility of the whole. Nemoto *et al.* have developed unileg TE modules based on n -type Mg_2Si [35,36]. This architecture is certainly more robust and reliable than a two-leg architecture since there is no problem of thermal expansion mismatch between the two TE materials, but the achieved TE performance is of course less.

In this paper, we present the manufacturing of silicide-based TE modules from TE materials prepared by an industrial process. We introduce a new design to minimize the thermomechanical issues, by developing ‘half-skeleton’ modules. Twenty-two such TE modules made of two pairs (n/p) legs were manufactured, and their performance tested in term of output power. The repeatability module to module was excellent while the achieved areal output power lies within the state of the art compared to other modules fabricated either with silicides or other TE materials working in the same temperature range (skutterudites, half-Heuslers, ...). Among all these materials, the silicides have the lowest cost/kg [22,23] which gives a competitive advantage for our modules. The TE performances of our TE modules as function of temperature are also compared with analytical and numerical models.

2. Experimental

2.1. Thermoelectric materials and legs preparation

The raw powders used in this study were produced in large quantities, ten kilograms per batch for each type of material, with the targeted n -type composition $\text{Mg}_2\text{Si}_{0.6}\text{Sn}_{0.4}$ doped with 1.35 wt% Sb (further called MSS) and p -type composition $\text{MnSi}_{1.77}$ (further called HMS). They were obtained from the melting of commercial powders of Mg (99%), Si (99.9%), Sn (99.9%), Sb (99.9%) and Mn (99%) followed by ball milling. The powders were then densified by spark plasma sintering (SPS) in graphite dies under argon atmosphere. The materials were held at 750 °C during 5 min under 50 MPa and at 1030 °C during 5 min under 55 MPa for the n - and p -types, respectively. The obtained pellets (60 mm in diameter and about 5.5 mm in thickness) were further annealed in an oven under argon atmosphere for 2 h at 450 °C and 900 °C for the n - and p -type materials, respectively. They were rectified mechanically under oil down to a thickness of 4.60 ± 0.02 mm, corresponding to the height of the thermoelectric legs, using a AC-530 Peter-Wolters machine. A metallic multi-layer constituted of Ti (30 nm)/Au (335 nm) was deposited on the lower and upper faces of the rectified pellets by magnetron sputtering (ALCATEL DP28). Finally, the pellets were cut in TE legs of dimensions $3 \times 3 \times 4.6 \text{ mm}^3$ with a wire saw under oil and with a micro-chain saw for the MSS and HMS materials, respectively. About 250 legs can be produced in one sintered pellet. Prior to their integration in a thermoelectric module, the resistance of all the legs was measured in order to eliminate any leg showing too much variation with regard to the mean value, resulting for instance from an unexpected contact resistance. For the HMS material, the mean resistance value is 8.3 m Ω , with a standard deviation of 2%, while it is 2.1 m Ω with a standard deviation of 13% for the MSS material. The lower resistance value results from the lower intrinsic resistivity (as will be seen later) while the higher standard deviation is due to the presence of some composition inhomogeneities in the material as it has already been shown by Mejri et al. [37]. Finally, all the legs issued either from a HMS or a MSS pellet have been qualified. Knowing the position of the leg in the pellet, neither edge-center nor shading effects have been observed, showing the reliability of the SPS fabrication process, even for a diameter as large as 60 mm.

2.2. Module design and assembly

This TE module model produced by HBOB is composed of 24 TE legs (Fig. 1a), i.e. of 12(n (MSS)/ p (HMS)) pairs, prepared as previously described. The originality of these modules lies in their ‘half-skeleton’ structure with the cold side conventionally linked to a ceramic plate but with the hot side linked to a thin silver foil acting as the electrode. This design ensures flexibility at the hot side such as to counterbalance the mismatch of thermal expansion coefficients between HMS and MSS, as mentioned in the introduction. In order to facilitate the study of reliability and repeatability tests, modules constituted of only two n/p couples have been fabricated in this study (Fig. 1b). Twenty-two of such modules have been manufactured according to the process flow described in Fig. 2.

Prior to the assembly, the n and p metallised TE legs, the AlN ceramic plates and the silver electrodes have been cleaned with acetone and absolute ethanol in an ultrasonic bath. The first assembly step consists in applying a commercial silver brazing paste by screen printing on the cold side electrodes made of nickel-coated copper tracks deposited on an aluminium nitride (AlN) ceramic substrate by the direct bonding copper (DBC) technique. Thanks to a pick & place machine, the legs are placed on the silver braze (step 2). Silver braze is then applied on the top of the TE legs (step 3), and finally the top silver electrode foils are automatically placed on the legs (step 4), consisting in the hot side of the module. The whole module is further placed in a thermo-press at 250 °C under 43 MPa for 30 min in air to sinter the brazing paste and ensure the final

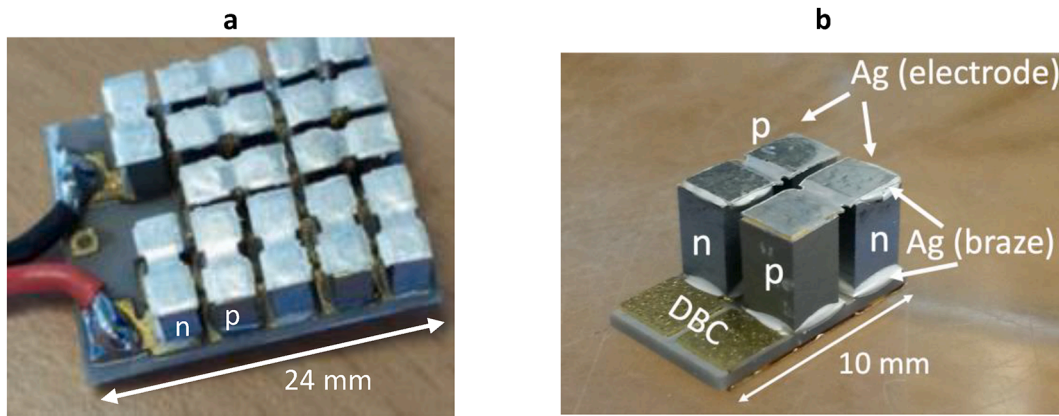


Fig. 1. Configuration of the TE modules made of (a) 12 HMS/MSS couples and (b) 2 HMS/MSS couples.

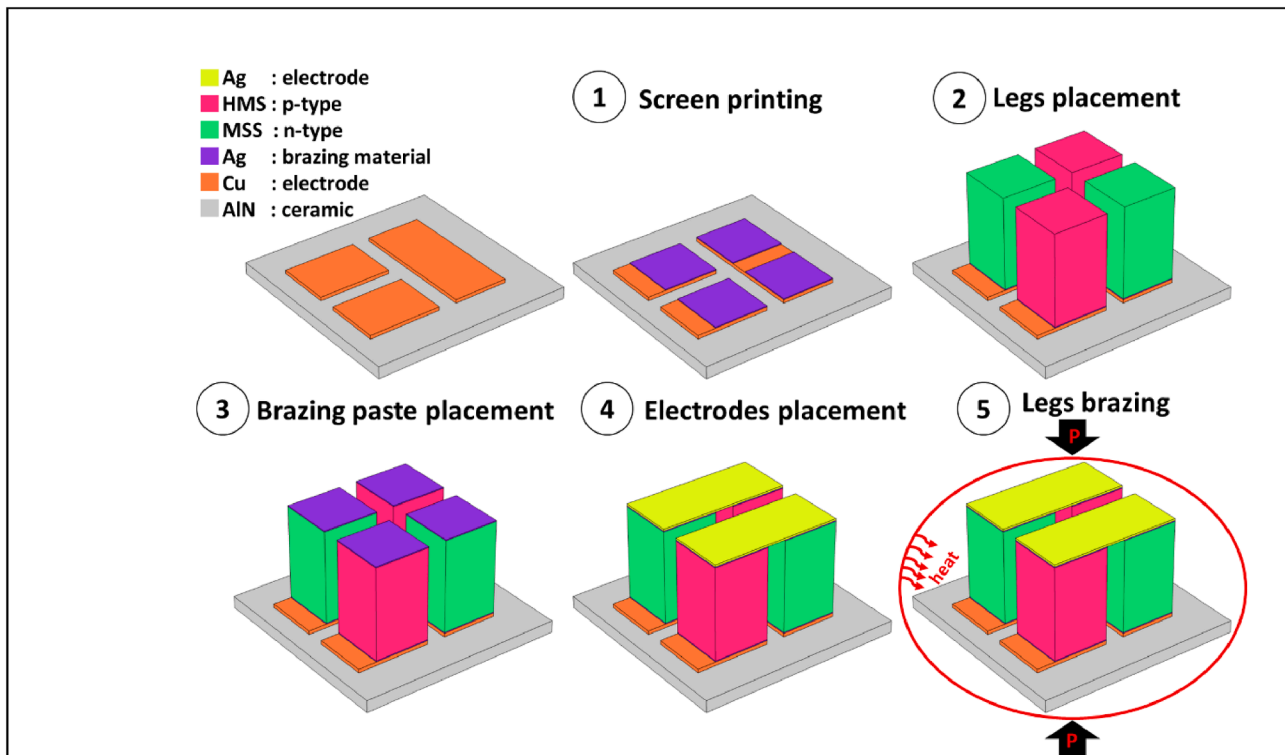


Fig. 2. Manufacturing process of the 2 HMS/MSS couples TE modules.

assembly of the different parts (step 5).

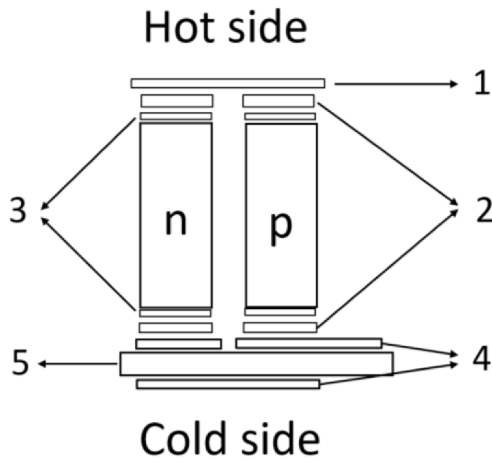
Fig. 3 shows a general scheme of the final structure of the fabricated TE modules., with the different interfaces in presence and their thickness.

2.3. Microstructural and TE characterizations of the materials

The apparent densities of the SPS sintered HMS and MSS samples were measured using the Archimedes method, in distilled water and absolute ethanol, respectively. The quality of the interfaces at the different leg/electrode junctions of a polished assembled TE module was checked by scanning electron microscopy (SEM) in the back-scattered electron mode (BSE) and elemental X-ray mapping on a Quanta FEG 650 (FEI) instrument.

The TE properties of the HMS and MSS materials were investigated in the 25–700 °C temperature range on different sintered samples. Samples of appropriate shape were cut from the non-metallized SPS pellets. The

electrical conductivity (σ) and the Seebeck coefficient (S) were measured simultaneously with a four-probe method using a ZEM-3 (ULVAC GmbH) apparatus on parallelepipedic-shaped samples of $3 \times 3 \times 12 \text{ mm}^3$ in size under helium atmosphere. The thermal conductivity (κ) was calculated from experimental data of the thermal diffusivity (D), specific heat (C_p), and density (d) using the equation $\kappa = DC_p d$. The thermal diffusivity was measured by a laser flash method (LFA 457 MicroFlash, NETZSCH GmbH) on square-shaped samples of 10×10 and 1 mm^3 in thickness, under argon. The specific heat was measured by differential scanning calorimetry (DSC 404 F1 PEGASUS, NETZSCH GmbH) on disk-shaped samples of 5.2 mm in diameter and 1 mm in thickness, under argon atmosphere. The dimensionless thermoelectric figure of merit ZT was estimated from the data of the three previous parameters. The measurement error of all the transport properties is no more than $\pm 5\%$.



- 1 – Ag electrode (125 μm)
- 2 – Ag braze (10-20 μm)
- 3 – Ti (30 nm)/Au (335 nm) metallic layers
- 4 – Ni (3-7 μm) coated Cu (200 μm) electrode
- 5 – AlN ceramic plate (635 μm)

Fig. 3. Expanded view of a TE module (one n/p couple) as built according to the process flow described in Fig. 2.

2.4. Module performance measurement

The performance of each of the twenty-two fabricated TE modules was measured on a dedicated test bench [38] developed in collaboration with OMICRON (Eybens, France). The measurement takes place inside a vacuum chamber allowing controlling the atmosphere during the test. A controlled hot temperature is applied at the top side of the TE module thanks to a heating ceramic element and a cold temperature at the bottom side thanks to a water cooling system. The hot temperature is

measured with a K-type thermocouple directly in contact with the top side of the TE module. The cold temperature is measured with a K-type thermocouple inside a copper buffer located between the cold side of the module and the water cooler chuck. Our measurement tests have been carried out under an atmosphere of 10 mbar of nitrogen while applying a mechanical pressure of 1 MPa on the module with the help of a pneumatic piston in order to lower the thermal contact resistance. As well, a thermal grease is used between the module, the copper buffer and the water cooler chuck so as to ensure minimal thermal contact resistance.

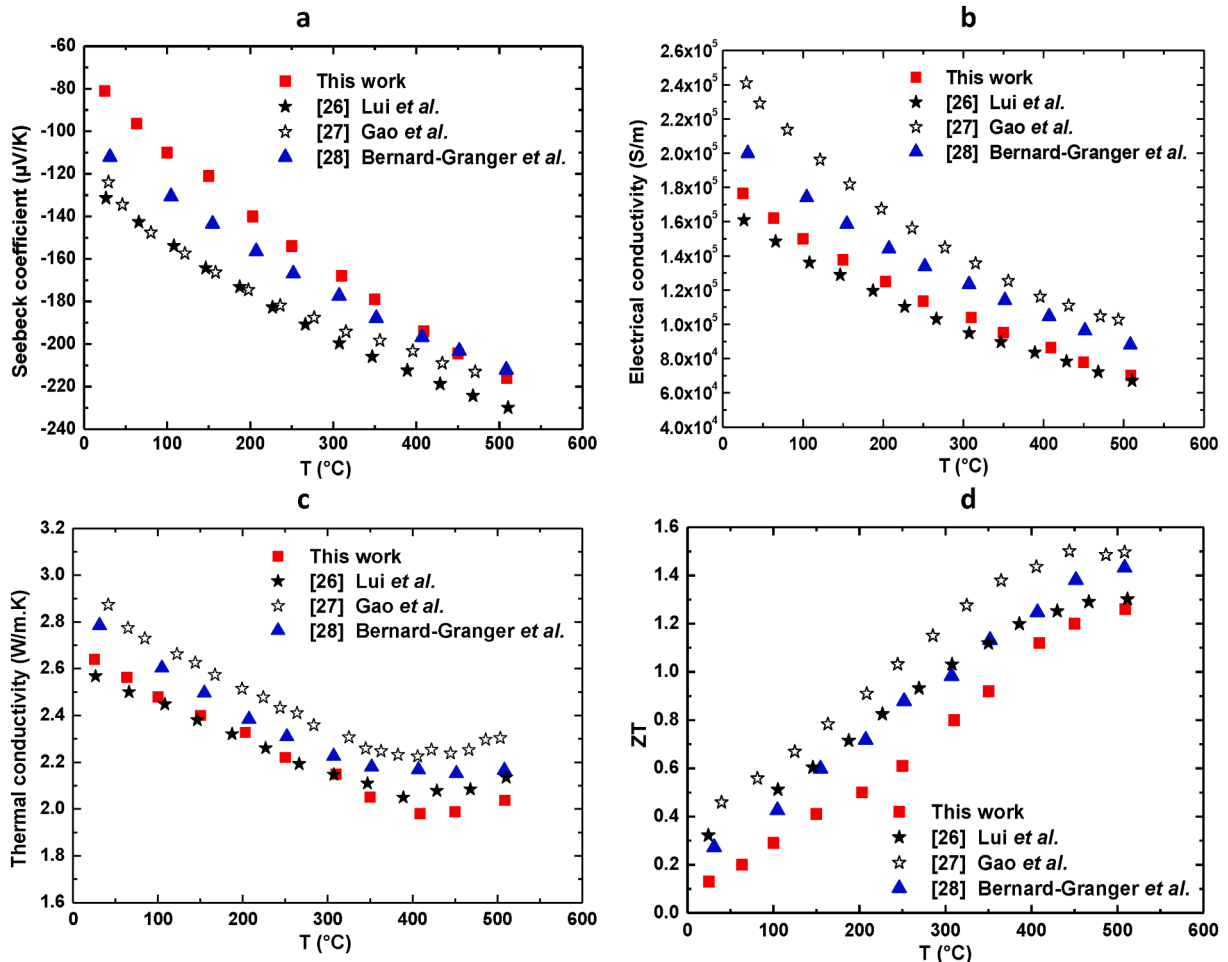


Fig. 4. Temperature dependences of a) Seebeck coefficient, b) Electrical conductivity, c) Thermal conductivity, and d) Figure of merit of MSS TE materials.

The cold temperature has been fixed to 50 °C. Once the temperature is stabilized, current is injected (Keithley 2651 A, 0.1% accuracy) and the voltage is measured to give the characteristic voltage versus current curve. The open circuit voltage V_{OC} , internal resistance R_{int} , and maximum output P parameters have been determined for hot side temperatures from 100 °C up to 450 °C, with a step of 50 °C. The measurements were quickly recorded (50 points in 1 s), avoiding thus any parasitic Peltier effect.

3. Results and discussion

3.1. Characterization of the TE materials

The sintered samples are dense, in agreement with the relative density values obtained of 5.1 g/cm³ (96% of the theoretical value) and 2.3 g/cm³ (99% of the theoretical value) for the HMS and MSS materials, respectively. The chemical composition and homogeneity, the crystalline structure and the microstructure as well as the thermomechanical properties of the SPS consolidated pellets of both the HMS and MSS materials used within this work have been already studied [33,37].

The measurement of the TE properties were carried out on several samples cut from different HMS and MSS sintered pellets, in order to check the reproducibility pellet to pellet. For both materials, the differences in between the pellets are very small, showing again the good control of the SPS process. The temperature dependences of the electrical conductivity, Seebeck coefficient, thermal conductivity, and figure of merit ZT of the MSS and HMS materials are shown in Figs. 4 and 5, respectively. They are compared with the best data reported so far in the literature for TE materials of similar composition.

The Seebeck coefficient of MSS is negative in the entire temperature range (Fig. 4a), indicating a n -type conduction, while that of HMS is positive (Fig. 5a), indicating a p -type conduction, both in good agreement with what was expected. The Seebeck coefficient values of our MSS material increases in absolute value from 81 μ V/K at 20 °C to 216 μ V/K at 500 °C, reaching the values achieved by Bernard-Granger et al. [28] and Gao et al. [27] but around 6% lower than those of Liu et al. [26]. For the HMS material, the Seebeck coefficient increases from 130 μ V/K at 20 °C to 231 μ V/K at 500 °C. These values are very close to the values reported by Bernard-Granger et al. [32] and slightly above that of Luo et al. [30,31].

The temperature dependence of the electrical conductivity of both MSS (Fig. 4b) and HMS (Fig. 5b) materials exhibit the typical behavior of a degenerated semiconductor. As can be observed, the electrical conductivity values of both our materials are lower compared to the values reported in the literature. These discrepancies may be due to the difference of chemical composition with regard to our alloys. Indeed, the n -type alloy used by Gao et al. [27] has a higher tin content compared to our MSS materials. On the other hand, the HMS alloy used in our work is not doped while the best materials reported in the literature are usually Al or Ge-doped [30–32].

The behavior of the thermal conductivity with temperature follows similar trends as those previously reported in the literature, for both MSS (Fig. 4c) and HMS (Fig. 5c).

The maximum values of the dimensionless TE figure of merit ZT (Figs. 4d and 5d) are 1.26 and 0.5 at 500 °C for the MSS and HMS materials, respectively. For the MSS material, this value is very close to the highest values ever reported in the literature for the Mg₂Si_{0.6}Sn_{0.4} (Sb doped) composition. Even if in the case of the HMS material, the

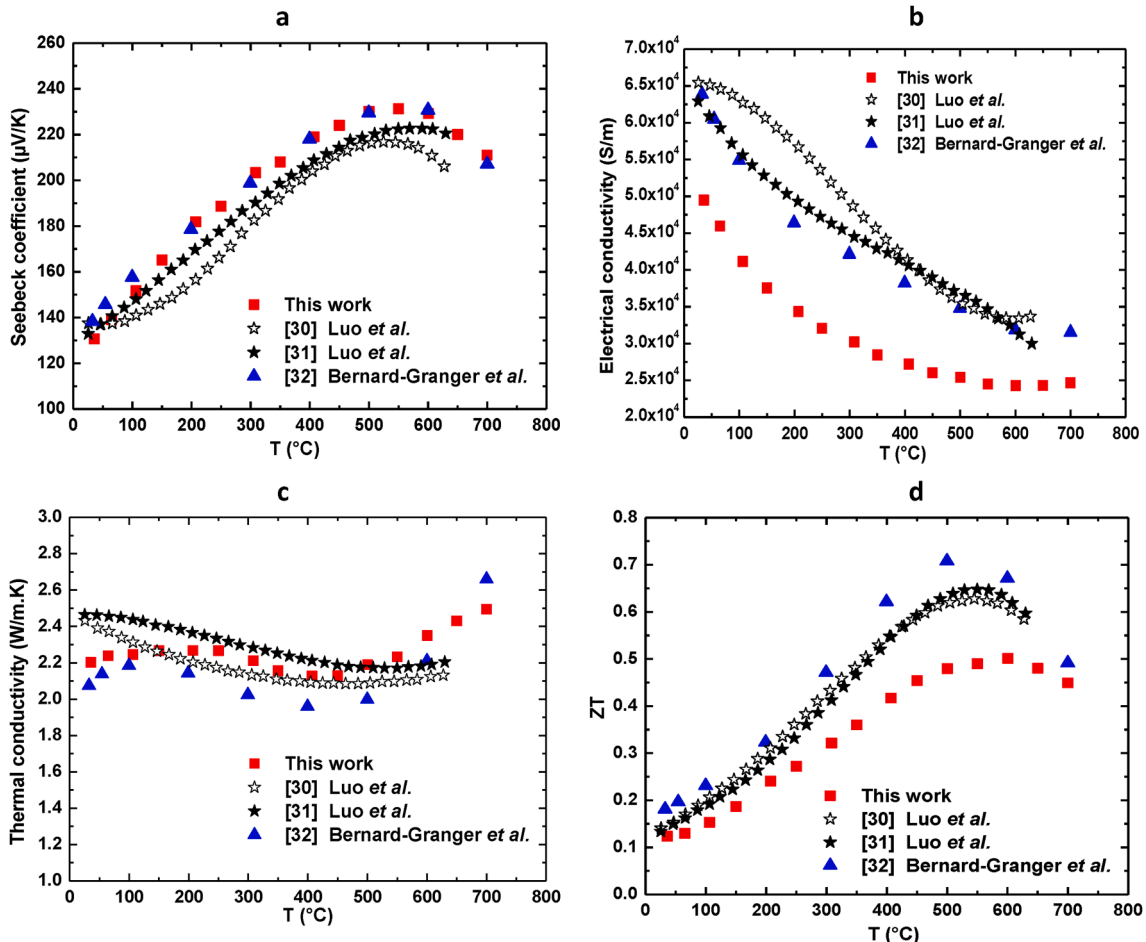


Fig. 5. Temperature dependences of a) Seebeck coefficient, b) Electrical conductivity, c) Thermal conductivity and d) Figure of merit of HMS TE materials.

maximum ZT achieved is slightly lower than the best values reported in this family of materials (ZT_{\max} 0.6–0.7 at 500 °C, [30–32]), it is still highly acceptable regarding the way of fabrication. Indeed, going from laboratory production (some grams of material) to mass production (some kilograms) is often unfavorable for the TE performance. Our materials, manufactured using three simple metallurgic methods (melting, ball milling and SPS), offer the advantage to combine mass production with TE performance fully compatible with state of the art performance.

3.2. Characterization and performance of the modules

3.2.1. Module interfaces

In Figs. 6 and 7 are reported SEM micrographs of the interfaces between the electrode layer/brazing layer/TE legs on the cold and hot sides of TE modules just after fabrication, for HMS and MSS TE legs, respectively. The brazing layers have a thickness of about 10 to 15 μm . Nor porosity, nor cracks or oxygen could be found at the different interfaces. The interfaces can be considered as perfect on both hot and cold sides of the module, corresponding perfectly to the scheme of Fig. 3, as it is highlighted on the overlays of all elemental X-rays mappings, whatever the material is (Figs. 6b, d, 7b, 7d). No diffusion in between the

different elements has been observed.

3.2.2. TE performance of the modules

In Fig. 8 are reported typical current–voltage and current–power curves measured on the 22 fabricated TE modules for a cold side temperature of 50 °C and hot side temperatures from 100 °C up to 500 °C (with 50 °C steps). The voltage (U) follows Ohm’s law according to:

$$U = V_{oc} - R_{int} \cdot I \quad (1)$$

where I is the current, R_{int} the internal electrical resistance and V_{oc} the open-circuit voltage.

Hence, the electrical power ($P = U \cdot I$) is given by:

$$P = R_{int} \cdot I^2 + V_{oc} \cdot I \quad (2)$$

The obtained voltage–current and power–current measured curves follow the expected behaviors given by Eqs. (1) and (2), linear and parabolic, respectively. From these measured curves are extracted the open circuit voltage V_{oc} (ordinate at the origin of the voltage–current curve), the internal resistance R_{int} (slope of the voltage–current curve), and the maximum electrical power output P_{max} (maximum value of the power on the power–current curve). In Fig. 9 are reported the measured V_{oc} , R_{ints} and P_{max} parameters versus the hot

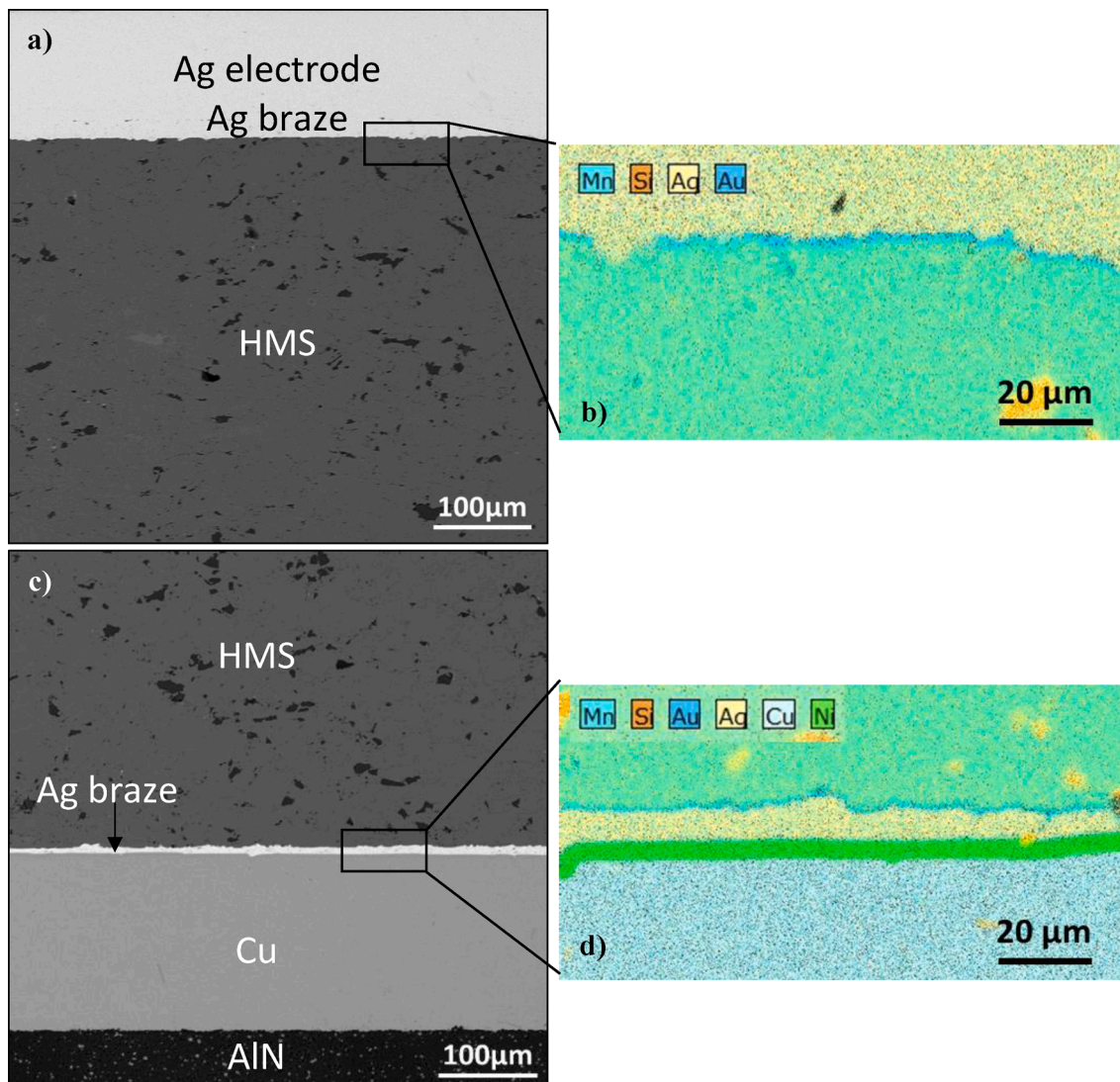


Fig. 6. SEM micrographs (BSE mode) of the interfaces of (a) hot side and (c) cold side of a HMS leg in a TE module. Zoom on the interfaces of (b) hot and (d) cold sides with overlays of elemental X-ray mappings of the elements mentioned on the images.

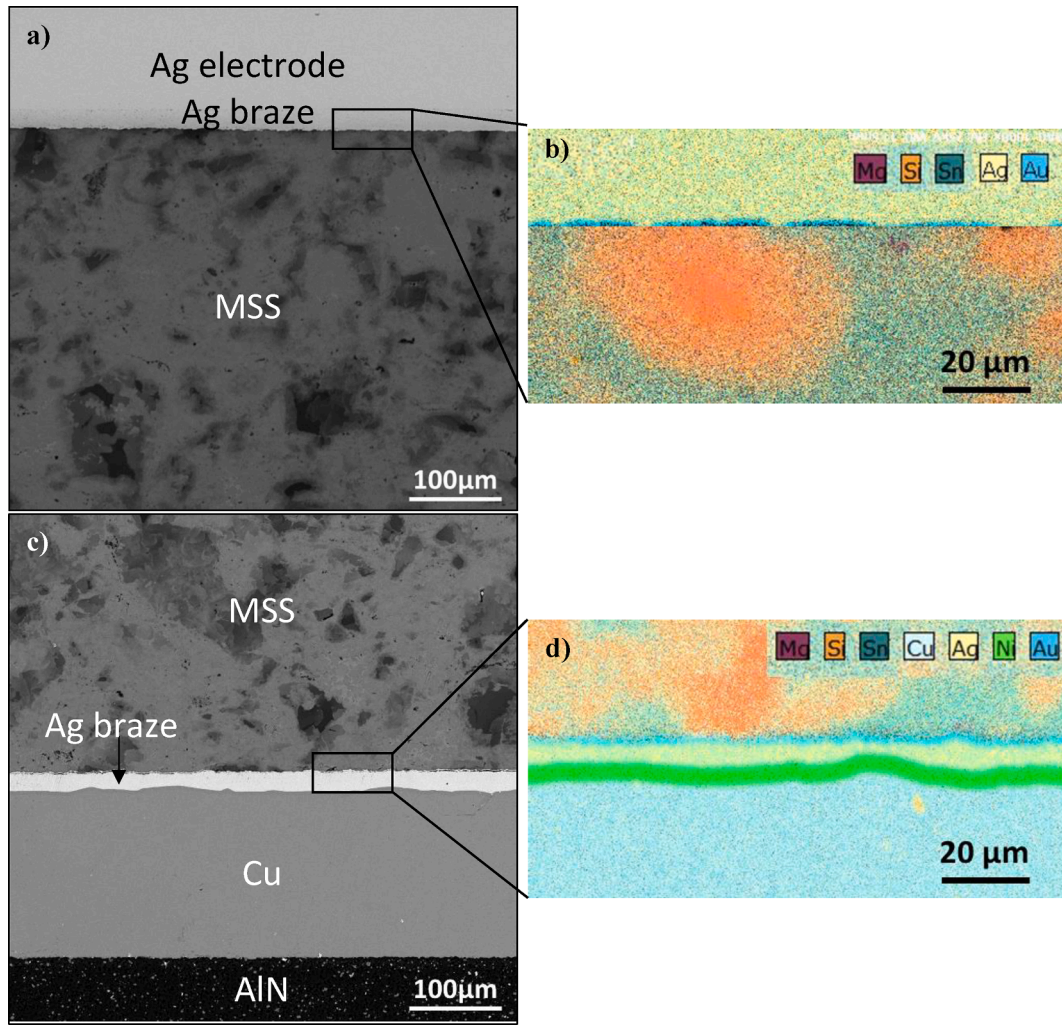


Fig. 7. SEM micrographs (BSE mode) of the interfaces of (a) hot side and (c) cold side of a MSS leg in a TE module. Zoom on the interfaces of (b) hot and (d) cold sides with overlays of elemental X-ray mappings of the elements mentioned on the images.

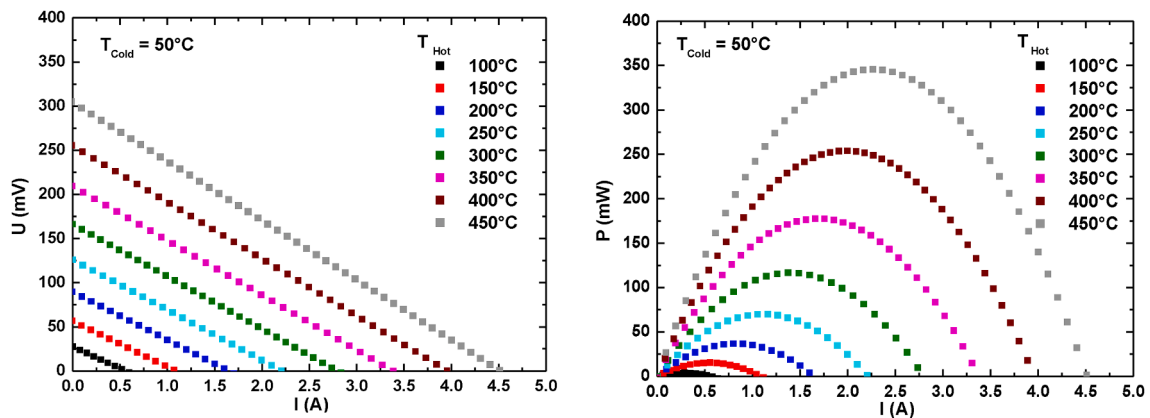


Fig. 8. Typical voltage-current (left) and power-current (right) characteristics measured on one of the 22 fabricated TE modules ($T_{\text{cold}} = 50\text{ }^{\circ}\text{C}$, T_{hot} from 100 to 450 $^{\circ}\text{C}$ by 50 $^{\circ}\text{C}$ step).

temperature for all 22 fabricated TE modules. One can see that each parameter exhibits a remarkable reproducibility module to module.

The open circuit voltage is the voltage generated by a module by the Seebeck effect. It is ideally equal to:

$$V_{oc} = N_{leg} S \Delta T \quad (3)$$

where N_{leg} is the number of legs, S the mean measured value of the Seebeck coefficient between the n and p-type TE materials and ΔT the temperature difference between the hot and cold sides.

If we compare the V_{oc} values obtained by this analytical model and the experimental values, a very good match is observed (Fig. 9a),

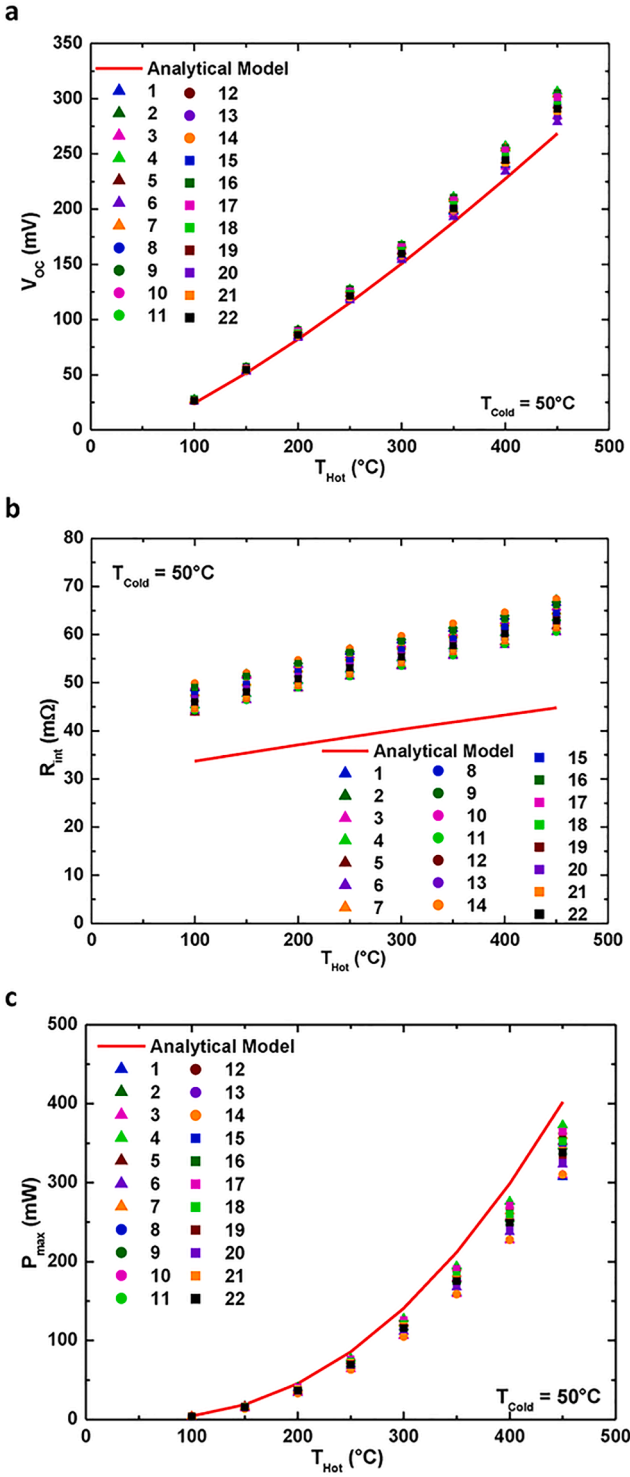


Fig. 9. a) Measured open-circuit voltage (V_{oc}), b) internal electrical resistance (R_{int}), and c) maximal power output (P_{max}) as a function of the hot side temperature for all the twenty-two TE modules.

meaning that our test bench does not add any significant thermal contact resistance, thanks to the pneumatic piston system and the use of thermal grease. Moreover, it shows that there is no significant temperature jump between both the DBC substrate and the TE legs on the cold side and the silver electrodes and the TE legs on the hot side of the TE module. Our TE module assembly process is thus validated in terms of thermal functionality.

In a similar way, the internal electrical resistance is directly linked to

the electrical resistivity, and is ideally equal to:

$$R_{int} = N_{leg} \rho \frac{h_{leg}}{A_{leg}} \quad (4)$$

where h_{leg} is the leg height, A_{leg} is the leg cross section and ρ the mean measured value of the electrical resistivity between the n- and p-type TE materials.

A good match between the ideal case and the measured values is also observed for the R_{int} parameter (Fig. 9b), meaning that the electrical resistance between the TE legs and the electrical tracks is very low. The TE module assembly is also thus validated in terms of electrical functionality.

Taking into account Eqs. (3) and (4), the Ideal maximum generated electrical power is equal to:

$$P_{max} = \frac{N_{leg}}{4} \frac{S^2 \Delta T^2}{\rho} \frac{A_{leg}}{h_{leg}} \quad (5)$$

A good match between the ideal values and the measured value is also obtained for the P_{max} parameter (Fig. 9c). Hence, no significant losses are to be deplored and almost all the heat conversion performed by the TE material is available in the TE module. The TE modules generate a maximum power of 0.35 W corresponding to a power areal density of 0.95 W/cm² (total area of the TE legs = 36 mm²) for a temperature difference of 400 °C (cold side at 50 °C). Table 1 provides a statistic overview of the generated power at different temperature conditions.

3.2.3. Finite elements performance modelling

To predict the performance of the fabricated modules, modelling by three-dimensional finite-elements analyses implemented in the COMSOL Multiphysics software has been used. The employed method has been already described [39]. However, as the temperature differences studied here are greater than those described in the paper where bismuth telluride-based modules were studied, we introduced in the modelling the actual measured temperature-dependent values of the material properties, fitted using third-order polynomials. The simulations were conducted on modules whose dimensions correspond to the fabricated ones. The boundary conditions were set to 50 °C at the cold side and from 100 to 450 °C at the hot side. Electrical contact resistances on the hot and cold sides (between the Ti/Au metallization and the TE material) were introduced into the simulation, estimated to be 38 μOhm·cm² and 17 μOhm·cm² for the p- and n-type materials, respectively. These electrical contact resistance values were calculated through the shift of the measured electrical resistance of individual legs with and without metallization. An external load resistance, connected to the generator to realize closed-circuit operation, was varied giving rise to various electric currents.

From the results of the simulation, it is possible to represent the temperature and voltage distributions in the studied generators as well as the current density and heat flux fields obtained for a load resistance that we have chosen equal to 65 mΩ (Fig. 10). The isotherms and

Table 1

Statistic values for the power output compiled for the twenty-two fabricated TE modules.

Temperature (°C)			P_{max} (W/cm ²)				
T_{Cold}	T_{Hot}	ΔT	Min	Max	Mean	Standard deviation	
50	100	50	0.009	0.012	0.011	0.001	5.8%
	150	100	0.039	0.047	0.044	0.002	5.4%
	200	150	0.093	0.113	0.103	0.006	5.3%
	250	200	0.176	0.214	0.196	0.010	5.3%
	300	250	0.292	0.354	0.324	0.017	5.2%
	350	300	0.441	0.539	0.490	0.026	5.3%
	400	350	0.630	0.767	0.698	0.037	5.3%
	450	400	0.853	1.036	0.949	0.050	5.3%

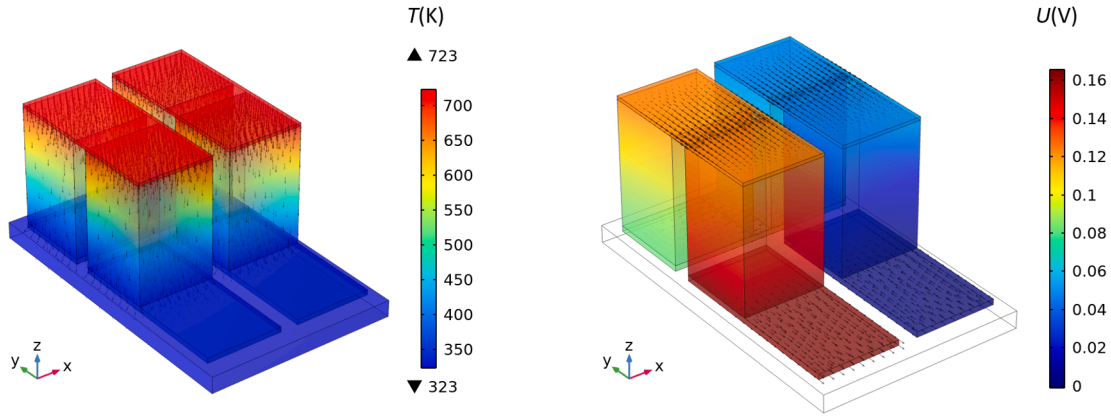


Fig. 10. Temperature (a) and voltage (b) distributions calculated by three-dimensional finite element analyses on two couples of *n*-MSS and *p*-HMS for an illustrative $T_{hot} = 723$ K and $R_{load} = 65$ m Ω . The arrows on the schemes correspond to the direction of heat flow and current density. Their length on the figures is proportional to the represented parameter.

equipotentials are obtained in the thermoelectric materials parallel to their surface and therefore only depend on the variable of dimension *z*. Likewise, the load and heat flows are directed through the legs in the *z* direction.

The evolution of the electrical output power as a function of the load resistance (which corresponds to a variation in current) is plotted in Fig. 11a. The maximum power is obtained when the load resistance is equal to the internal resistance of the generator. This maximum is shifted slightly towards a higher load resistance as the temperature increases, linked to a greater internal resistance (Figs. 4a and 5b). The electrical power increases steadily with the temperature at the hot side, reaching a maximum value of 0.70 W for a temperature difference of 500 °C (0.43 W for a temperature difference of 400 °C). In Fig. 11b are compared the experimental mean values of the electrical power determined from the twenty-two modules, with data obtained either by numerical (ideal condition) or analytical modelling. The simulated values are higher than the experimental values, the difference increasing with the temperature of the hot side. For $T_{hot} = 450$ °C, the power loss is of the order of 25%. This loss is assumed to be due to the electrical contact between the solder and metallized TE legs. These results show that there are still some improvements to be made to have a perfect electrical contact at all solder interfaces, which is still a challenge for the experimenter.

3.2.4. Comparison with state of the art

The performance of our thermoelectric modules is compared with

the state-of-art in Fig. 12. The chosen parameter is the generated electrical power (P_{max}), which is the key parameter for a ThermoElectric Generator system, when waste heat is used. All values have been normalized with respect to the cross-sectional area of the thermoelectric

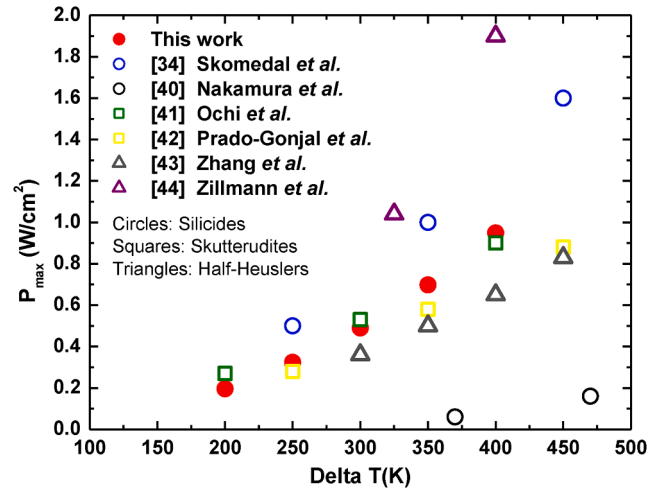


Fig. 12. TE modules performance versus the state-of-art in the medium temperature range (200–500 °C).

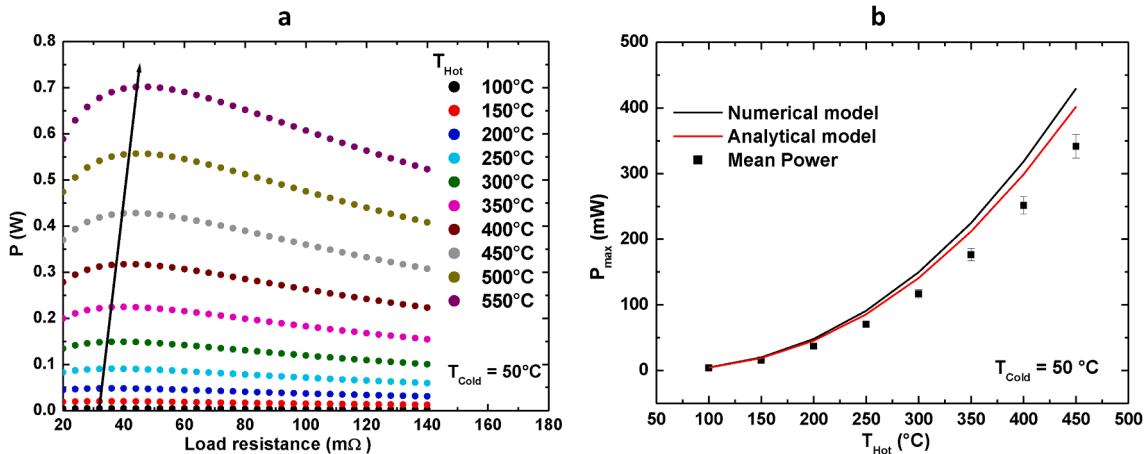


Fig. 11. (a) Power output as a function of the load resistance for different hot side temperatures (the arrow crosses the maximums), (b) mean maximal power output (P_{max}) as a function of temperature obtained from all twenty-two fabricated TE modules compared with numerical and analytical modelling.

elements in order to have an accurate comparison between modules with different designs. The comparison is performed with the best published results describing thermoelectric modules working at a medium temperature range (200–500 °C) including different non-conventional thermoelectric materials (silicides [34,40], skutterudites [41,42] and Half-Heuslers [43,44]). The performances of our TE modules are in line with previous published results, compared either with silicide-based modules or with other materials-based modules, even using an industrial process for the TE materials production and the module assembly. Among all these materials, the silicides have the lowest cost/kg [22,23] which gives a competitive advantage for our modules. A mean value of 4.4% has been estimated for the TE efficiency at a temperature difference of 400 °C (hot side temperature of 450 °C). Decreasing the electrical contact resistance remains a great challenge in order to achieve better performance.

4. Conclusion

In this work, silicide-based TE modules have been manufactured on the base of a new design, called 'half skeleton', with the aim to manage the differences of thermal expansion between the *n*-type ($\text{Mg}_2\text{Si}_{0.6}\text{Sn}_{0.4}$) and *p*-type ($\text{MnSi}_{1.77}$) TE materials thanks to the presence of a flexible silver electrode located at the hot side of the modules. Indeed, no deterioration is to be deplored during the performance tests carried out up to 450 °C on any of the twenty-two modules made of two (*n/p*) couples tested. Such very promising result was achieved thanks to the optimization of each step of the process fabrication allowing mass production of TE modules. Special emphasis must be placed on the SPS step that allowed obtaining more than 200 perfectly reproducible TE legs. SEM analyses show that the different interfaces between the electrodes /brazing layer/TE legs are free of any defect (crack, diffusion, ...) whatever the side or the material is. An average maximum power output of 0.37 W, corresponding to a power density of 0.95 W/cm², has been achieved for a temperature difference of 400 °C (hot side temperature of 450 °C). This performance lies our modules within the state of the art, albeit the TE materials have been produced by 10 kg batches, for foreseen applications in the mid-range temperature (200–500 °C). The COMSOL modelling has shown that still some amelioration can be brought by solving the delicate problem of electrical contact resistance as the maximum power extracted represents around 86% of the expected value. Long-term stability tests at a given temperature and under given cycling conditions are to be performed in different working atmospheres in order to further validate our design. Such tests are underway, as well as the search for innovative coatings.

CRediT authorship contribution statement

H. Ihou Mouko: Methodology, Investigation, Writing - review & editing, Supervision, Project administration. **K. Romanjek:** Methodology, Investigation, Writing - review & editing, Supervision, Project administration. **M. Mejri:** Methodology, Investigation, Writing - review & editing. **M. Oulfarsi:** Methodology, Investigation, Writing - review & editing. **S. El Oualid:** Methodology, Investigation. **P. Malinconi:** Methodology, Investigation. **Y. Thimont:** Methodology, Investigation, Writing - review & editing, Supervision. **B. Malard:** Methodology, Investigation, Writing - review & editing, Supervision. **C. Estournès:** Methodology, Investigation, Writing - review & editing, Supervision, Project administration. **N. David:** Methodology, Investigation, Writing - review & editing, Supervision, Project administration. **A. Dauscher:** Methodology, Investigation, Writing - review & editing, Supervision, Project administration.

Declaration of Competing Interest

The authors declare that they have no known competing financial interests or personal relationships that could have appeared to influence

the work reported in this paper.

Acknowledgements

This work was supported by the French National Research (ANR-16-CE05-0012-03), within the RELIATEG (Reliable Thermoelectric Generators) project. It allowed funding two PhDs in Materials Sciences; Mahdi MEJRI at Université Toulouse III - Paul Sabatier (Toulouse, France) and Mostafa OULFARSI at Université de Lorraine (Nancy, France).

References

- [1] Saidur R, Rezaei M, Muzammil WK, Hassan MH, Paria S, Hasanuzzaman M. Technologies to recover exhaust heat from internal combustion engines. *Renew Sust Energy Rev* 2012;16(8):5649–59. <https://doi.org/10.1016/j.rser.2012.05.018>.
- [2] R.L. Cataldo, G.L. Bennett, U.S. Space radioisotope power Systems and Applications: Past, Present and Future. In: *Radioisotopes - Applications in Physical Sciences*, N. Singh, editor. InTech, pp 473-496 (2011), doi: 10.5772/23914.
- [3] Holgate TC, Bennett R, Hammel T, Caillat T, Keyser S, Sievers B. Increasing the efficiency of the multi-mission radioisotope thermoelectric generator. *J Electron Mater* 2015;44(6):1814–21. <https://doi.org/10.1007/s11664-014-3564-9>.
- [4] Brignone M, Zigiotti A. Impact of novel thermoelectric materials on automotive applications. *AIP Conf Proc* 2012;1449:493. <https://doi.org/10.1063/1.4731601>.
- [5] C. Bode, J. Friedrichs, R. Somdalen, J. Kohler, K.D. Büchler, C. Falter, U. Kling, P. Ziolkowski, K. Zabrocki, E. Müller, D. Kozulovic, Potential of future thermoelectric energy recuperation for aviation, *J. Enginee. Gas Turbines Power*, 139, 101201 (2017), doi: 10.1115/1.4036527.
- [6] Luo Qi, Li P, Cai L, Zhou P, Tang Di, Zhai P, et al. A Thermoelectric Waste-Heat-Recovery System for Portland Cement Rotary Kilns. *J Elect Mater* 2015;44(6): 1750–62. <https://doi.org/10.1007/s11664-014-3543-1>.
- [7] Hudak NS, Amatucci GG. Small-scale energy harvesting through thermoelectric, vibration, and radiofrequency power conversion. *J Appl Phys* 2008;103(10): 101301. <https://doi.org/10.1063/1.2918987>.
- [8] Haras M, Skotnicki T. Thermoelectricity for IoT – A review. *NanoEnergy* 2018;54: 461–76. <https://doi.org/10.1016/j.nanoen.2018.10.013>.
- [9] He R, Schierning G, Nielsch K. Thermoelectric devices: a review of devices, architectures, and contact optimization. *Adv Mater Tech* 2018;3(4):1700256. <https://doi.org/10.1002/admt.v3.410.1002/admt.201700256>.
- [10] Wu W, Ren G-K, Chen X, Liu Y, Zhou Z, Song J, et al. Lin, Interfacial advances yielding high efficiencies for thermoelectric devices. *J Mater Chem A* 2021;9(6): 3209–30. <https://doi.org/10.1039/D0TA06471H>.
- [11] Freer R, Powell AV. Realising the potential of thermoelectric technology: a roadmap. *J Mater Chem C* 2020;8(2):441–63. <https://doi.org/10.1039/C9TC05710B>.
- [12] Champier D. Thermoelectric generators: a review of applications. *Energy Convers Manage* 2017;140:167–81. <https://doi.org/10.1016/j.enconman.2017.02.070>.
- [13] Goldsmid H. Bismuth telluride and its alloys as materials for thermoelectric generation. *Materials* 2014;7(4):2577–92. <https://doi.org/10.3390/ma7042577>.
- [14] Rogl G, Rogl P. Skutterudites, a most promising group of thermoelectric materials. *Curr Opin Green Sustain Chem* 2017;4:50–7. <https://doi.org/10.1016/j.cogsc.2017.02.006>.
- [15] Poon SJ. Recent advances in thermoelectric performance of Half-Heusler compounds. *Metals* 2018;8:989. <https://doi.org/10.3390/met8120989>.
- [16] Moshwan R, Yang L, Zou J, Chen Z-G. Eco-friendly SnTe thermoelectric materials: Progress and future challenges. *Adv Funct Mater* 2017;27(43):1703278. <https://doi.org/10.1002/adfm.v27.4310.1002/adfm.201703278>.
- [17] Li W, Wu Y, Lin S, Chen Z, Li J, Zhang X, et al. Advances in environment-friendly SnTe thermoelectrics. *ACS Energy Lett* 2017;2(10):2349–55. <https://doi.org/10.1021/acsenenergylett.7b00658>.
- [18] Fedorov MI. Thermoelectric silicides: past, present and future. *J Thermoelectr* 2009;2:51.
- [19] Pandel D, Banerjee MK, Singh AK. A review of the Mg₂(Si, Sn) alloy system as emerging thermoelectric material: experimental and modeling aspects. *J Electron Mater* 2021;50(1):25–51. <https://doi.org/10.1007/s11664-020-08591-z>.
- [20] Beretta D, Neophytou N, Hodges JM, Kanatzidis MG, Narducci D, Martin-Gonzalez M, et al. From history, a window to the future. *Mater Sci Eng R* 2019;138: 100501. <https://doi.org/10.1016/j.mser.2018.09.001>.
- [21] Schierning G, Chavez R, Schmechel R, Balke B, Rogl G, Rogl P. Concepts for medium-high to high temperature thermoelectric heat-to-electricity conversion: a review of selected materials and basic considerations of module design. *Transl Mater Res* 2015;2(2):025001. <https://doi.org/10.1088/2053-1613/2/2/025001>.
- [22] Amatya R, Ram RJ. Trend for thermoelectric materials and their earth abundance. *J Electron Mater* 2012;41(6):1011–9. <https://doi.org/10.1007/s11664-011-1839-y>.
- [23] LeBlanc S, Yee SK, Scullin ML, Dames C, Goodson KE. Material and manufacturing cost considerations for thermoelectrics. *Renew Sust Energy Rev* 2014;32:313–27. <https://doi.org/10.1016/j.rser.2013.12.030>.
- [24] W. Liu, K. Yin, Q. Zhang, C. Uher, X. Tang, Eco-friendly high-performance silicide thermoelectric materials, *National Sci. Rev.*, 4, 611 (2017), doi: 10.1093/nsr/nwx011.

- [25] G. Kim, H. Shin, J. Lee, W. Lee, A review on silicide-based materials: Thermoelectric and mechanical properties, *Met. Mater. Inter.* (2020), in press, doi: 10.1007/s12540-020-00609-9.
- [26] Liu W, Tang X, Li H, Sharp J, Zhou X, Uher C. Optimized thermoelectric properties of Sb-doped $Mg_{2(1+z)}Si_{0.5-y}Sn_{0.5}Sb_y$ through adjustment of the Mg content. *Chem Mater* 2011;23(23):5256–63. <https://doi.org/10.1021/cm202445d>.
- [27] Gao P, Berkun I, Schmidt RD, Luzenski MF, Lu Xu, Bordon Sarac P, et al. Transport and mechanical properties of high-ZT $Mg_{2.08}Si_{0.4-x}Sn_{0.6}Sb_x$ thermoelectric materials. *J Electron Mater* 2014;43(6):1790–803. <https://doi.org/10.1007/s11664-013-2865-8>.
- [28] Bernard-Granger G, Navone C, Leforestier J, Boidot M, Romanjek K, Carrete J, et al. Microstructure investigations and thermoelectrical properties of an N-type magnesium–silicon–tin alloy sintered from a gas-phase atomized powder. *Acta Mater* 2015;96:437. <https://doi.org/10.1016/j.actamat>.
- [29] J. de Boor, U. Saparamadu, J. Mao, K. Dahal, E. Müller, Z. Ren, Thermoelectric performance of Li doped, p-type $Mg_2(Ge,Sn)$ and comparison with $Mg_2(Si,Sn)$, *Acta Mater.*, 120, 273 (2016), doi: 10.1016/j.actamat.2016.08.057.
- [30] Luo W, Li H, Yan Y, Lin Z, Tang X, Zhang Q, et al. Rapid synthesis of high thermoelectric performance higher manganese silicide with in-situ formed nanophase of MnSi. *Intermetallics* 2011;19(3):404–8. <https://doi.org/10.1016/j.intermet.2010.11.008>.
- [31] Luo W, Li H, Fu F, Hao W, Tang X. Improved thermoelectric properties of Al-doped Higher Manganese Silicide prepared by a rapid solidification method. *J Electron Mater* 2011;40(5):1233–7. <https://doi.org/10.1007/s11664-011-1612-2>.
- [32] Bernard-Granger G, Soulier M, Ihou-Mouko H, Navone C, Boidot M, Leforestier J, et al. Microstructure investigations and thermoelectrical properties of a P-type polycrystalline higher manganese silicide material sintered from a gas-phase atomized powder. *J Alloys Compd* 2015;618:403–12. <https://doi.org/10.1016/j.jallcom.2014.08.164>.
- [33] Mejri M, Thimont Y, Malard B, Estournès C. Characterization of the thermo-mechanical properties of p-type ($MnSi_{1.77}$) and n-type ($Mg_2Si_{0.6}Sn_{0.4}$) thermoelectric materials. *Acta Mater* 2019;172:28–32. <https://doi.org/10.1016/j.scriptamat.2019.06.037>.
- [34] Skomedal G, Holmgren L, Middleton H, Eremin IS, Isachenko GN, Jaegle M, et al. Design, assembly and characterization of silicide-based thermoelectric modules. *Ener Convers Manage* 2016;110:13–21. <https://doi.org/10.1016/j.enconman.2015.11.068>.
- [35] Nemoto T, Iida T, Sato J, Sakamoto T, Hirayama N, Nakajima T, et al. Development of an Mg_2Si unileg thermoelectric module using durable Sb-doped Mg_2Si legs. *J Electron Mater* 2013;42:2192. <https://doi.org/10.1007/s11664-013-2569-0>.
- [36] Nemoto T, Iida T, Sato J, Suda H, Takanashi Y. Improvement in the durability and heat conduction of uni-leg thermoelectric modules using n-type Mg_2Si legs. *J Electron Mater* 2014;43(6):1890–5. <https://doi.org/10.1007/s11664-013-2897-0>.
- [37] Mejri M, Malard B, Thimont Y, Romanjek K, Ihou Mouko H, Estournès C. Thermal stability of $Mg_2Si_{0.55}Sn_{0.45}$ for thermoelectric applications. *J Alloys Compd* 2020;846:156413. <https://doi.org/10.1016/j.jallcom.2020.156413>.
- [38] Romanjek K, Vesin S, Aixala L, Baffie T, Bernard-Granger G, Dufourcq J. High-performance silicon-germanium-based thermoelectric modules for gas exhaust energy scavenging. *J Electron Mater* 2015;44(6):2192–202. <https://doi.org/10.1007/s11664-015-3761-1>.
- [39] El Oualid S, Kosior F, Dauscher A, Candolfi C, Span G, Mehmedovic E, et al. Innovative design of bismuth-telluride-based thermoelectric micro-generators with high output power. *Energy Environ Sci* 2020;13(10):3579–91. <https://doi.org/10.1039/D0EE02579H>.
- [40] Nakamura T, Hatakeyama K, Minowa M, Mito Y, Arai K, Iida T, et al. Power-generation performance of a pi-structured thermoelectric module containing Mg_2Si and $MnSi_{1.73}$. *J Electron Mater* 2015;44:3592. <https://doi.org/10.1007/s11664-015-3910-6>.
- [41] Ochi T, Nie G, Suzuki S, Kikuchi M, Ito S, Guo JQ. Power-generation performance and durability of a skutterudite thermoelectric generator. *J Electron Mater* 2014;43(6):2344–7. <https://doi.org/10.1007/s11664-014-3060-2>.
- [42] Prado-Gonjal J, Phillips M, Vaquero P, Min G, Powell AV. Skutterudite thermoelectric modules with high volume-power density: Scalability and reproducibility. *Appl Energy Mater* 2018;1(11):6609–18. <https://doi.org/10.1021/acsam.8b01548.s001>.
- [43] Zhang Y, Cleary M, Wang X, Kempf N, Schoensee L, Yang J, et al. High-temperature and high-power-density nanostructured thermoelectric generator for automotive waste heat recovery. *Energy Convers Manage* 2015;105:946–50. <https://doi.org/10.1016/j.enconman.2015.08.051>.
- [44] Zillmann D, Metz D, Matheis B, Dietzel A, Waag A, Peiner E. Thermoelectric generators fabricated from large-scale-produced Zr-/Hf-based Half-Heusler compounds using Ag sinter bonding. *J Electron Mater* 2019;48(9):5363–74. <https://doi.org/10.1007/s11664-019-07366-5>.